








Martian Dust Devil Detection Based on Improved Faster R-CNN

Zexin Guo , Yi Xu , *Member, IEEE*, Dagang Li , Yemeng Wang , Kim-Chiu Chow , Renrui Liu ,
and Qiquan Yang 

Abstract—A dust devil is an important part of the Martian climate system, which can help us better understand scientific questions of the climate, surface–atmosphere interactions, aeolian processes, and regolith on Mars. Therefore, the automatic detection of dust devils from Mars orbiter images is becoming increasingly important for the scientific study and the planning of future robotic and manned missions. To improve the generalization, detection efficiency, and accuracy of the traditional approach in automatically detecting dust devils, we made several modifications to the faster region-based convolution neural network. Based on the characteristics of the dust devil, we proposed a Martian dust devil detection network (MDDD Net). The network uses the feature pyramid network to obtain a feature fusion map with rich location information and semantic information. The k-means++ algorithm is used to design reasonable anchor boxes to adapt to vary sized dust devils. The region of interest align unit is introduced to eliminate the mapping deviation between the feature map and the original image. Finally, the soft nonmaximum suppression algorithm is used to complete the screening of the bounding box. It can reduce missing detections caused by the overlapping between adjacent dust devil bounding boxes in the same image. The average precision and recall of MDDD Net on the dust devil dataset built in this article reach 90.1% and 96.5%, respectively.

Index Terms—Dust devil, faster region-based convolution neural network (faster R-CNN), feature pyramid network (FPN), K-means++, Mars, region of interest align (ROI align), soft nonmaximum suppression (soft-NMS).

I. INTRODUCTION

THE suspended dust on Mars is an important part of the Martian climate system. As early as the 18th century, people used telescopes to observe the presence of “yellow clouds or

Manuscript received 28 November 2023; revised 28 January 2024; accepted 9 February 2024. Date of publication 29 February 2024; date of current version 10 April 2024. This work was supported in part by the Pre-Research Project on Civil Aerospace Technologies of China National Space Administration under Grant D020101, in part by the Science and Technology Development Fund of Macau under Grant 0010/2023/AFJ, in part by the National Natural Science Foundation of China 42201389, and in part by Guangdong-Hong Kong-Macao Greater Bay Area International Scientific and Technological Innovation Cooperation Project under Grant 2021A0505030080. (*Corresponding author: Yi Xu.*)

Zexin Guo, Yi Xu, Yemeng Wang, Kim-Chiu Chow, and Renrui Liu are with the State Key Laboratory of Lunar and Planetary Sciences, Macau University of Science and Technology, Macau 999078, China (e-mail: a1025922331@163.com; yixu@must.edu.mo; ymwang8@outlook.com; kc-chow@must.edu.mo; liurenruis@gmail.com).

Dagang Li is with the International Institute of Next Generation Internet, Macau University of Science and Technology, Macau 999078, China (e-mail: dagang.li@ieee.org).

Qiquan Yang is with the State Key Laboratory of Lunar and Planetary Sciences, Macau University of Science and Technology, Macau 999078, China, and also with the College of Surveying and Geo-Informatics, Tongji University, Shanghai 200092, China (e-mail: yangqiqquan@must.edu.mo).

Digital Object Identifier 10.1109/JSTARS.2024.3367848



Fig. 1. Dust devil appeared in the Amazonis Planitia shot by HiRISE camera.

hazes” on the surface of Mars [1], [2]. With more and more data coming back from Mars missions, our understanding of Mars has become more comprehensive. According to the observed spatial and temporal scales and difference in morphology, dust clouds can be divided into two categories: dust storms and dust devils. The spatial scale of dust storms can range from local to the planetary scale, and the duration of dust storms can range from days to months. In contrast, dust devils (see Fig. 1) have some distinct morphological characteristics, they are also small in size and have a short lifespan. Although individual dust devils are local events, they are widespread on a global scale. This indicates that the dust devils play an important role in the Martian dust cycle [3], [4]. The formation process of Martian dust devils is similar to that of the dust devils on Earth. Both are caused by a small-scale convection movement in the near-surface air layer due to strong local warming of the ground. It can lift dust on the surface of Mars into the air, forming a dust column and wandering on the ground for a few minutes.

Various studies on Mars in recent years have shown that Mars has a much more dynamic surface environment than we previously thought. Among them, the Martian atmosphere has an extremely dynamic process of change. As a dynamic event, the Martian dust devil can provide us with a lot of useful information for studying the atmosphere of Mars. Insight into Martian dust events can help us better understand scientific questions about climate, surface–atmosphere interaction, low atmospheric behavior, aeolian processes, and regolith in Mars [5], [6]. For example, the frequency, size diversity, and effective dust-lifting ability of dust devils indicate that they play an important role in the thermal structure of the atmospheric boundary layer of Mars [7]. The seasonal changes of the dust devils’ track streaks found in Noachis are consistent with the seasonal “wave of darkening” observed by the orbital camera, which indicates that

dust devils and dust storms are important contributors to the seasonal “wave of darkening” phenomenon [3]. The seasonal trend of the Martian dust devil height is similar to that of the planetary boundary layer height, which indicates that the shadow of the dust cyclone can provide key information, such as the wind direction and the planetary boundary layer height related to the lower atmosphere [8]. By analyzing the speed, directions of motion, and general characteristics of the dust devils observed in the high-resolution stereo camera (HRSC), dust devils are considered to have an important contribution to the entrainment of dust into the atmosphere and the Martian dust cycle [9]. In addition, dust devils and dust storms may also pose a greater threat to the landing of the Mars rover. In May 1971, the Soviet Mars III probe failed to land due to a dust storm on the surface of Mars. Therefore, an overall understanding of the temporal and spatial distribution of dust devils and other characteristics will also help us to better plan future Mars exploration programs. The real-time automatic detection of dust devils can also help the rover automatically avoid dangerous dust devils when landing.

As an event of high scientific research value, Martian dusty devils began to receive more and more attention. Because dust devils are relatively rare and have low temporal and spatial scales, it is not easy to observe them. Fortunately, with the continuous upgrading of Mars detection technology, we have been able to see the clearer images of Martian dust devils, which include not only the imaging of the orbital detection cameras but also the imaging of the ground-based probes. Active dust devils were first observed by Viking Orbiter cameras, which are bright small clouds with long cone-shaped shadows [10] and were also observed on other Mars orbiters subsequently: Mars global surveyor Mars orbiter camera [11], Mars Odyssey thermal emission imaging system [12], Mars express HRSC [13], Mars reconnaissance orbiter (MRO) Mars color imager, MRO context camera (CTX), and MRO high-resolution imaging experiment camera (HiRISE) [14]. Observational data from the orbiter provide key information for understanding the sizes, heights, speeds, geographical distribution, and seasonal changes of dust devils. However, due to the limitation of the local time of the orbiter [3], [11], the diurnal variability characteristics of the dust devils need to be observed by surface detectors. Several active dust devils were found and tracked in Mars pathfinder, Mars exploration rover (MER) spirit, MER opportunity, Phoenix Mars rover, and Mars Science Laboratory curiosity [15], [16], [17], [18], [19], [20]. Scientists have carried out a series of studies on dust devils based on the above image data.

With the continuous development of the Mars exploration program, we have accumulated a large number of high-resolution images from orbital probes and surface probes for analysis. Among them, MRO CTX has taken more than 126 000 images of the Martian surface with high-definition resolution and wide coverage. Because the amount of image dataset is too large and only a small part of it contains active dust devils, using the traditional artificial visual search method to find continuously generated dust devils is not only inefficient but also inaccurate (some dust devils with unobvious features are difficult to be recognized by humans).

Previously, a dust devil’s motion detection algorithm based on background subtraction has been applied to the images shot by the MER spirit rover, which can help detect faint dust devils that are not detectable by the naked eye [21]. However, compared with the orbiter images, the lander images are limited by the field of view and the height above the ground; hence, it is difficult to estimate the dust devil heights, distances, speeds, and directions of movement. A Gaussian-based filter is applied to detect typical dust devils from the orbiter image [22], [23]. It builds a series of filters suitable for different light directions, different diameters, and different heights of dust devils, so the detection efficiency is relatively low. The dynamic behavior and morphological diversity of dust devils also lead to ever-changing dust devil images, which makes it difficult for Gaussian-based filters to apply to different morphologies of dust devils. In addition, because dust devils often leave dark and slender tracks on the surface, dust devils tracks are also often used to study active dust devils [4], [24]. However, studies have indicated that only a small part of dust devils can produce stripes by destroying and removing surface dust [3]. The formation and preservation of dust devil tracks are affected by the horizontal speeds of dust devils, the properties of the substrate, and the thickness of the dust layer on the top of the substrate [25], [26]. Therefore, the data size and regional differences still limit the investigations of dust devil tracks to regional studies.

In recent studies, researchers have proposed a method using Cubesats and onboard scheduling to maximize the tracking observations of Martian dust devils [27]. Their research aims to improve the efficiency of dust devil observations on Mars by utilizing small satellites and efficient scheduling. They implemented a dust devil detection model using the CNN algorithm, achieving an average precision (AP) of 0.7. This study provides a novel approach for tracking dust devils on Mars.

Furthermore, there have been studies on plume tracking and related topics. For instance, researchers have proposed a model-based method for detecting plumes on comets that do not rely on machine learning techniques [28]. Their research automatically detects and tracks plumes on the 67P/Churyumov–Gerasimenko comet using OSIRIS/Rosetta image sequences. In addition, there have been studies on surface feature detection and tracking on small bodies using onboard computer vision techniques [29], [30]. These studies provide insights for tracking dust devils on other celestial bodies.

Moreover, there have been numerous studies on deep learning processing onboard satellites. Researchers have investigated the use of deep neural networks for satellite Earth observation [31]. Their research utilizes deep learning models onboard satellites for Earth observation and achieves good results. Furthermore, there have been studies evaluating the performance of deep learning models for space application [32]. These studies provide references for applying deep learning models for dust devil detection onboard satellites.

In order to solve the problems of poor generalization ability, low detection efficiency, and low accuracy of the traditional automatic detection algorithm of Martian dust devils, we made targeted improvements on the faster region-based convolution neural network (faster R-CNN) algorithm and proposed Martian

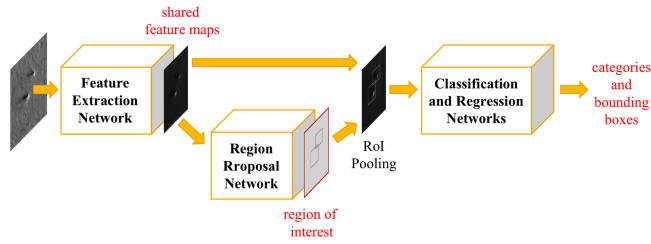


Fig. 2. Faster R-CNN network architecture diagram.

dust devil detection network (MDDD Net). The main improvements include adding a feature pyramid network (FPN), resetting preset anchor boxes, introducing a region of interest align (RoI align) unit, and soft nonmaximum suppression (soft-NMS) algorithm. In addition, we constructed a dataset for Martian dust devil object detection in view of the lack of Martian dust devil image data to verify the algorithm.

The rest of this article is organized as follows. Section II introduces the background of faster R-CNN. Section III describes the proposed improved methods in detail. The experimental and result analysis are given in Section IV. Finally, Section V concludes this article.

II. BACKGROUND ON FASTER R-CNN

Faster R-CNN is a two-stage object detection algorithm [33], and its biggest innovation is the proposed region proposal network (RPN). By sharing the convolutional feature layer, the RPN network and fast R-CNN are unified into one network, which solves the time-consuming problem of candidate box generation in the R-CNN and fast R-CNN algorithms, and greatly improves the efficiency of the two-stage detection algorithm.

The basic network architecture of faster R-CNN is shown in Fig. 2, which is mainly composed of a feature extraction network, RPN network, region of interest pooling (RoI pooling) unit, and classification and regression networks. In the specific implementation, the faster R-CNN algorithm first uses a convolutional neural network to extract features from the input image and obtain a feature map with high-level semantic information. The PRN network uses the feature map to generate anchor boxes, trains the anchor boxes, obtains the regions of interest, and gives the classification of whether the proposed area belongs to the foreground or the background. The classification and regression network is trained on the proposed region output by the RPN to classify and locate the objects in the proposed region.

As the basic network of faster R-CNN, the feature extraction network mainly uses a series of combined operations of convolution, activation, and pooling layers to extract image feature maps and provide them to the RPN layer and fast R-CNN module.

Generally speaking, a good feature extraction network has strong feature expression ability, which can provide great help for subsequent detection tasks. Therefore, the selection of a feature extraction network is particularly important. With the development of convolutional neural networks, more and better feature extraction networks are emerging. The most representative network models are Alex-Net, ZF-Net, VGG-Net, Google-Net [34], residual network (Res-Net) [35], and so on. After

referring to the advantages and disadvantages of each network model and analyzing the Martian dust devil detection task, we selected ResNet50 as the feature extraction network. Its network is deep and can extract more advanced features. The unique skip connection of deep Res-Net can make the information of the previous residual block flow into the next residual block without hindrance. It not only improves the information flow but also avoids the vanishing gradient problem and the degradation problem caused by the deep network.

III. PROPOSED MDDD NET

According to the characteristics of the Martian dust devil detection task, we have made the following improvements to the original faster R-CNN network and proposed an MDDD Net. Its network structure is shown in Fig. 3.

A. Multilayer Feature Fusion Based on FPN

The feature extraction network used in this subject is the ResNet50 network. The network structure is deep enough to learn advanced features. But in the original faster R-CNN, its feature extraction network only uses a single high-level feature layer as a shared convolutional feature layer for the subsequent RPN and fast R-CNN to use. This will cause an obvious issue. Some small-sized dust devil objects have less pixel information than large-sized ones, so their feature information is easily lost in the downsampling process. In order to solve the problem that the model is very sensitive to the difference in the size of the dust devil, we add an FPN design to the feature extraction network ResNet50, as shown in Fig. 4. By superimposing and connecting the feature maps of each connected feature layer in the feature extraction network, the FPN [36] solves the problem that small object features are blurred or even lost after multiple convolution and pooling operations.

1) *Bottom-Up Route*: In ResNet50 network convolution bottom-up, this process has {C1, C2, C3, C4, C5} five convolution layers.

2) *Top-Down Route*: In the FPN network, the feature information of {M4, M3, M2, M1} is upsampled from top to bottom using the nearest neighbor interpolation method to preserve the semantic information of the feature map to the greatest extent.

3) *Horizontal Connection Route*: Use a 1×1 convolution kernel to convolve each layer of the ResNet50 network and fuse the corresponding feature layers of the FPN network so as to obtain a feature map with both good spatial information and strong semantic information.

After the ResNet50 is fused with the FPN network, the convolution kernel needs to be used to convolve the P layer to reduce the aliasing effect caused by the nearest neighbor interpolation. Finally, the feature maps fused with different scales are provided to the subsequent network for use.

B. Anchor Boxes Design Based on K-Means++

In the original faster R-CNN algorithm, the anchor boxes (priori bounding boxes laid out in a grid) are combined according to different preset sizes and aspect ratios. The sizes are 128, 256,

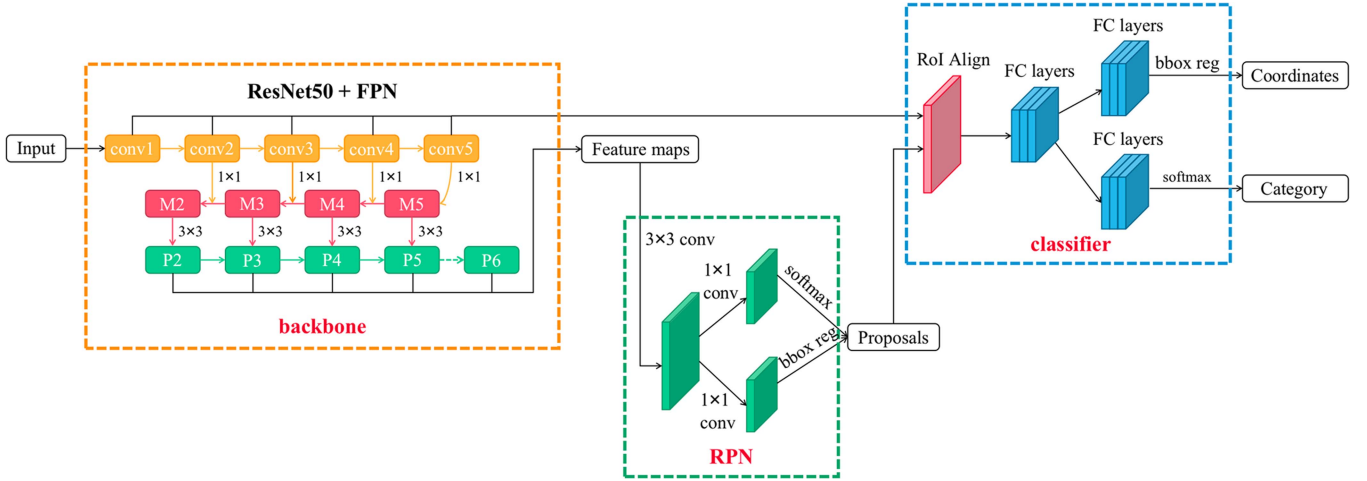


Fig. 3. Structure diagram of the MDDD Net.

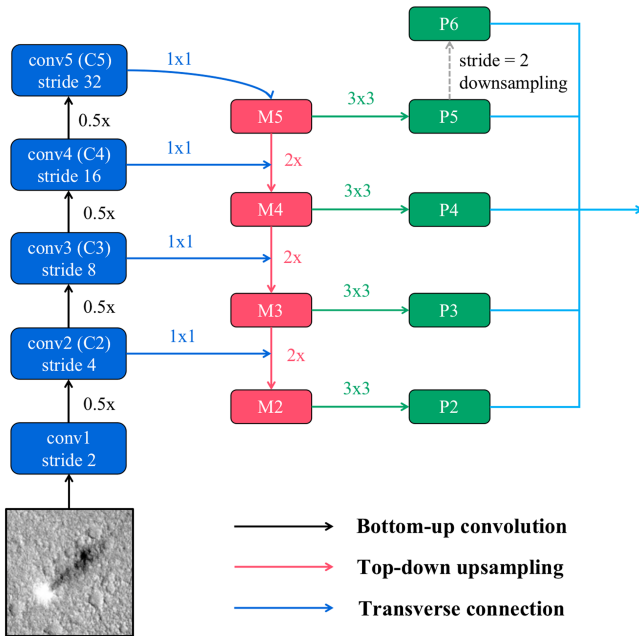


Fig. 4. Feature extraction network.

and 512, and the aspect ratios are 1:1, 1:2, and 2:1. However, this method generates too many suggested regions, and these parameters are not well adapted to the shapes and sizes of Martian dust devils, resulting in relatively slow training and testing processes. Therefore, it is necessary to choose a more appropriate set of anchor boxes to make the model easy to learn.

By using the K-means clustering algorithm to learn the sizes of the real object boxes, we obtained the shape distribution rule of the dust devil in the training set and reset the size of the anchor boxes. K-means clustering algorithm is a typical unsupervised learning algorithm, which uses distance as the similarity evaluation index, and is mainly used to divide n samples into k categories. The clustering process is shown as follows.

- 1) Extract and normalize the size of each real object box from the training set, including the area and aspect ratio of the object, and use this as the n input samples for the K-means clustering algorithm.
- 2) Set the number of categories to k and randomly select k points from the n samples as the center points of the first round of clustering.
- 3) Calculate the distance between n samples and k cluster centers, and cluster the n samples (each sample belongs to the category whose cluster center is closest to the cluster center). Finally, we calculate the mean of all samples for each cluster to get a new cluster center.
- 4) Repeat step (3) until the conditions for stopping iteration are met. The final k cluster centers are k prior anchor boxes.

In this task, we use (1) to define a new distance expression to calculate the similarity between sample points and center sample. GT is the real object box marked on the training set.

CE is the calculated cluster center; R_{IoU} is the quotient of the intersection (IoU) and union of GT and CE . The calculation method is shown in (2). The function $J(GT, CE)$ defined in the clustering process is shown in (3)

$$D(GT, CE) = 1 - R_{IoU}(GT, CE) \quad (1)$$

$$R_{IoU}(GT, CE) = \frac{S(GT \cap CE)}{S(GT \cup CE)} \quad (2)$$

$$J(GT, CE) = \sum_{i=1}^n D_i(GT, CE) \quad (3)$$

which represents the sum of the distances from all ground truth to the nearest cluster center. The stopping condition of the clustering process is to reach a certain number of iterations or the value of $J(GT, CE)$ does not change.

However, the traditional K-means algorithm also has certain defects. Its convergence speed and simplicity come at the expense of accuracy. There are many specific examples that the cluster centers generated by this algorithm do not achieve our desired results. Furthermore, these examples also show that the clustering results depend on the location of the starting cluster

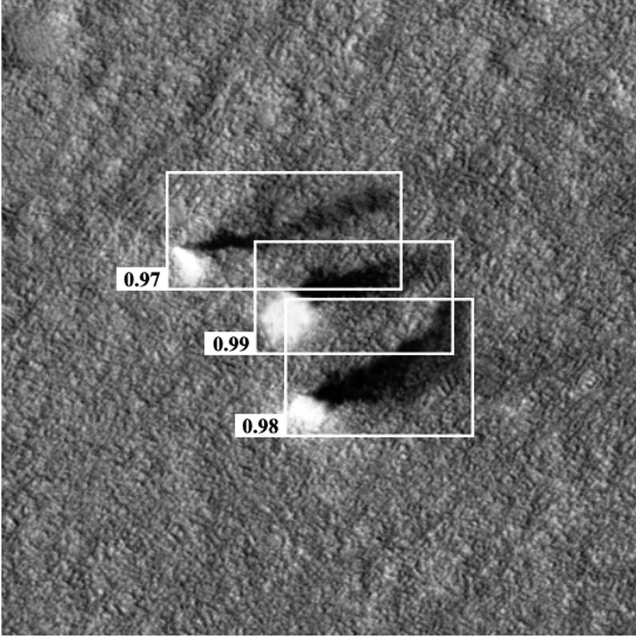


Fig. 5. Dense dust devils.

centers and that the use of standard random assignment of starting points makes the clustering results less robust.

In order to solve the above problems, we used K-means++ to replace K-means. The basic thought of K-means++ is to initialize the cluster centers by choosing random starting centers with probability function. The specific steps for selecting the initial cluster center point are shown as follows.

- 1) Randomly select a sample as the first cluster center c_1 .
- 2) Calculate the shortest distance between each sample and the current existing cluster centers (that is, the distance from the nearest cluster center), represented by $D(x)$.
- 3) The bigger the $D(x)$ value, the higher chance the sample being selected as the cluster center in this round.
- 4) Use the Roulette method to select the next cluster center.
- 5) Repeat steps (2)–(4) until k cluster centers are selected.

Through the probability function, we found that the cluster centers selected by the K-means++ algorithm are relatively scattered. This clustering algorithm achieved a better clustering effect than K-means. Therefore, in this project, we use the K-means++ algorithm for the anchor boxes of the Mars dust devil detection algorithm so that the anchor boxes can better adapt to the morphological characteristics of the dust devil. When $k = 5$, the clustering results are (26, 13), (41, 20), (63, 29), (97, 43), and (164, 75), which represent the heights and widths of the anchor boxes. These anchor boxes were applied to the feature maps of different scaled outputs from the FPN.

C. Candidate Boxes Filtering Based on Soft-NMS

In order to avoid repeated detection of the same object, faster R-CNN uses a nonmaximum suppression algorithm (NMS) to complete the selection of candidate boxes, which will suppress candidate boxes with Intersection over Union (IoU) value greater

than the threshold of the current candidate box. Hence, the NMS algorithm is sensitive to the setting of the threshold. If the threshold is too small, the candidate frame with a lower score will be completely suppressed by the adjacent high-scoring candidate boxes, which will lead to a high missed detection rate. If the threshold is too large, NMS cannot suppress duplicate detection boxes well, which will lead to duplication object detection. Therefore, the traditional NMS algorithm is prone to missed detection when dealing with multiple dust devils intensively occurring scenes.

As shown in Fig. 5, there is an overlap between the candidate boxes when multiple adjacent high-scoring dust devil candidate boxes are present. If the IoU threshold setting is unreasonable, the adjacent dust devil candidate boxes with relatively low score may be suppressed, resulting in the occurrence of missed detection.

To avoid this issue, we used soft-NMS [37] to replace NMS in faster R-CNN. In NMS, the score for candidate boxes with IoU value higher than the threshold will be set as 0, as shown in (4). In contrast, soft-NMS does buffering work and uses an attenuation function to adjust the score of the candidate box with an IoU value higher than the IoU threshold. The commonly used attenuation functions include linear weighting and Gaussian weighting. Linear weighting is used in this project, as shown in (5)

$$s_i = \begin{cases} s_i, & \text{iou}(M, b_i) \leq N_t \\ 0, & \text{iou}(M, b_i) \geq N_t \end{cases} \quad (4)$$

$$s_i = \begin{cases} s_i, & \text{iou}(M, b_i) \leq N_t \\ s_i(1 - \text{iou}(M, b_i)), & \text{iou}(M, b_i) \geq N_t. \end{cases} \quad (5)$$

D. Feature Maps Pooling Based on RoI Align

Since dust devils are small in size and often appear densely in images, the extraction accuracy of regions of interest is particularly critical for small and dense dust devil objects. The RoI pooling in faster R-CNN is used to map the candidate boxes generated by the RPN to the feature map output by the shared convolution layer to obtain the regional feature maps of the candidate regions. Finally, the regional feature maps are evenly divided into blocks according to the output requirements, and maximum pooling is performed on each block to generate fixed-size feature maps.

However, since RoI pooling includes two rounding operations, the region proposal box mapped on the feature map is biased. For example: Assuming that there is a candidate frame size of 88×88 in the original image, the size of the feature map obtained after the feature extraction network is reduced by 16 times (that is, it becomes 5.5×5.5). At this time, the first rounding will be performed, and the size of the obtained feature map will become 5×5 . Assuming that the subsequent network requires the input of a 2×2 fixed-size feature map, then RoI pooling will divide the 5×5 candidate area into 2×2 small blocks. The side length of each small block is $5/2 = 2.5$, that is, the small block size is 2.5×2.5 . At this time, the second quantization is performed, and the obtained small block size will actually become 2×2 . Finally, max pooling is performed

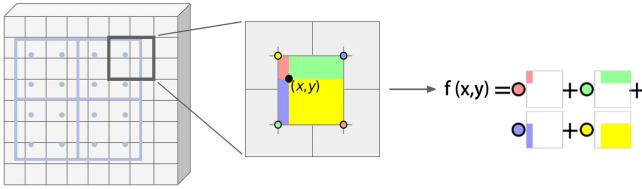


Fig. 6. Bilinear interpolation algorithm.

TABLE I
EXPERIMENTAL ENVIRONMENT DETAILS

Environment	Description
Operating system	Ubuntu 20.04.1 LTS
CPU	AMD Ryzen 7 3700X
GPU	NVIDIA TITAN RTX (24G)
Programming language	Python
Deep learning Infrastructure	Pytorch

in each small block to obtain a 2×2 feature map. From the above process, we can see that, after two rounding operations, the 5.5×5.5 regional feature map is actually mapped to a 4×4 local feature map. Such pixel deviation will definitely affect the regression positioning of the subsequent network, especially for small-sized dust devils.

For this problem, we use RoI align proposed in the mask R-CNN algorithm [38] to replace RoI pooling. It retains floating-point numbers and uses bilinear interpolation to calculate corresponding pixel values, which avoids the loss of precision caused by rounding and improves spatial symmetry.

When the same situation is handled in RoI align, since floating-point numbers are reserved, the 5.5×5.5 candidate frame feature map will be obtained after the first quantization, and the side length of the small block will become $2.75/2 = 2.75$ after the second quantization. Assuming that the sampling point is set to 4 (dividing each 2.75×2.75 block into four small cells), RoI align will use the bilinear interpolation algorithm to calculate the center pixel value of each small cell (see Fig. 6), and then take the maximum pixel value of these four sampled pixels as the pixel value of this small block (similar to max pooling). In this way, we can get a feature map of size 2×2 without mapping bias. Fig. 7 shows the process of feature map mapping and pooling for the above example using RoI pooling and RoI align, respectively.

IV. EXPERIMENTAL RESULTS AND ANALYSIS

A. Experimental Environment

The experimental platform used in this project is a desktop computer with AMD Ryzen 7 3700X processor and NVIDIA TITAN RTX (24G) graphics card graphics card (as shown in Table I). The operating system is Ubuntu 20.04.1 LTS. The development language is Python 3.6. The deep learning framework used is PyTorch.

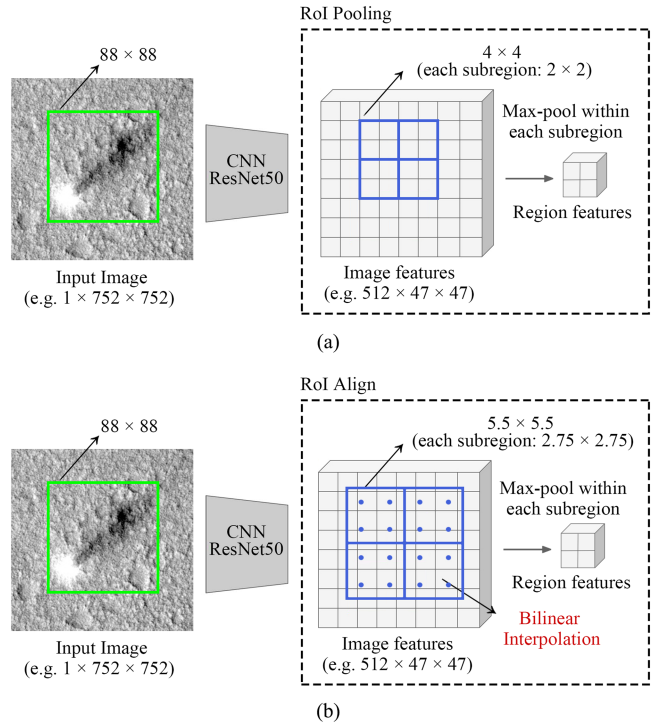


Fig. 7. Process of feature map mapping and pooling. (a) RoI pooling. (b) RoI.

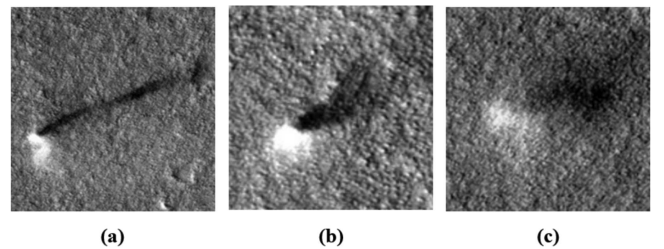


Fig. 8. Different morphologies of Martian dust devils. (a) Narrow, tightly defined column. (b) Inverted V-shaped dust cloud with a less well-defined column. (c) Poorly defined inverted V shape with no visible internal column.

B. Martian Dust Devil Detection Dataset

Since there is currently no authoritative and public Martian dust devil detection dataset available in the world, we used model iteration method to construct a VOC format dataset for Martian dust devil detection based on CTX images, which not only has a large number of dust devil samples (2315 objects) but also covers different morphologies of dust devils (see Fig. 8). The establishment of this dataset lays the foundation for preventing overfitting problems and improving the generalization ability of detection models.

The data source we selected is the CTX on the Mars exploration orbiter. The CTX camera primarily provides a context for high-resolution analysis of key spots on Mars provided by HiRISE and CRISM. Its image set covers almost the entire Martian surface and has an image resolution of up to 6 m/pixel, which makes it ideal for our mission. Previous studies have indicated that the Amazon Plain is a frequent place for dust

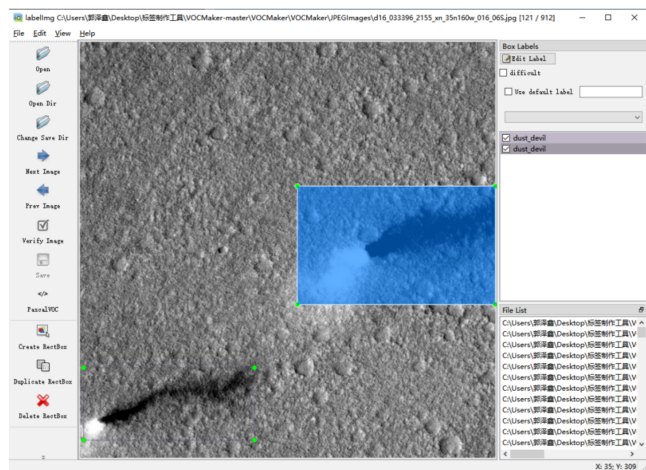


Fig. 9. Use the “labelImg” tool to mark the dust devil.

devils [3], [8], [39], so we used the CTX images of this area (W:140°–180°; N:0°–40°) to make a dataset.

First, from the official website (viewer.mars.asu.edu), we downloaded all the CTX images shot over the Amazonis Planitia so far, a total of 3958 images. Then, dozens of CTX images containing more dust devils were preliminarily screened out through artificial vision. In order to take into account the model’s requirements for the size of the input image and the retention of more details, we cut each large CTX image into hundreds of small images close to 750×750 pixels using the sliding window method. Next to use artificial vision for further screening to obtain 400 small images containing dust devils, and use the “labelImg” tool to mark the positions of the outer rectangles of these dust devil samples (see Fig. 9).

So far, we have constructed the initial detection network dataset. Through the first round of training, the initial results of the Martian dust devil detection model were obtained. Although the Martian dust devil detection model has been trained with 400 dust devil images, a small part of the dataset, they contain different morphologies of dust devils, which makes the model robust. By using the initial model, other images in the untrained dataset can be used to obtain the initial prediction box of the dust devils. The initial training dataset contains only 400 dust devil images, although most of the untrained images can be detected, a general model with strong generalization ability has not been obtained. Therefore, it is necessary to further expand the dataset to continue iterative training.

The initial detection model trained on 400 labeled dust devil images was used to detect the remaining untrained more than 500 000 small images, and the preliminary prediction results of the dust devil positions in the image were obtained. Through the inspection of the initial detection results, the bounding boxes of the wrongly detected image were corrected as the label of the target position in the image, and the expanded dataset after the initial training was obtained. Fig. 10(a) shows the predicted result by checking the initial detection model, and Fig. 10(b) shows the adjusted result.

After revising the prediction results of nearly 500 000 small images, a total of 2000 images of marked dust devils were

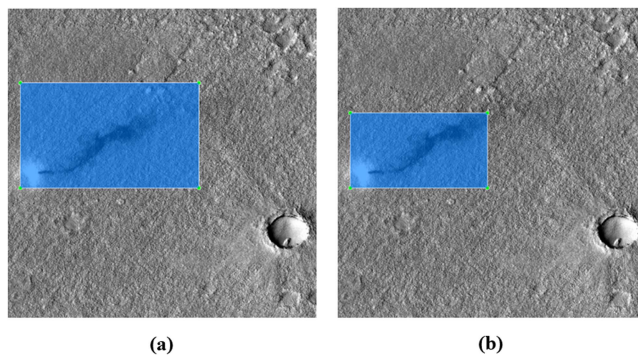


Fig. 10. Schematic diagram of detection frame correction. (a) Initial model. (b) Corrected image.

obtained (including 2315 multiscale and multimorphological dust devil objects), which were used as training sets to train the dust devil detection algorithm based on faster R-CNN. The method of preliminary prediction and iteration through the initial detection model can effectively reduce the workload of image screening and location marking. In addition, batch operations also ensure the accuracy and consistency of labeled data, which lays a good foundation for the final detection accuracy.

We have made this dataset publicly available on GitHub.¹

Restricted by the difficulty of data collection, the dataset we made is still difficult to meet the number of images required to optimize network parameters, which may easily lead to the situation that the model is not robust and the detection accuracy is not high. Therefore, in order to improve the robustness of the algorithm model, reduce overfitting, and improve detection accuracy, we can use data augmentation to expand the dataset. Data augmentation refers to the method of performing some changes on the training data to generate new effective data.

There are many methods of image enhancement, such as random cropping, mirroring, shifting, rotation, zooming, contrast transformation, and adding noise. However, in the specific practice process, the appropriate method should be selected according to the task requirements. After analyzing the original collected data and detection tasks, we chose shifting, rotation, and zooming to expand the original dataset, which is shown in Fig. 11. It enabled the Martian dust devil detection algorithm to learn more image-invariant features.

Finally, we selected 15% of the dataset as the test set, and the remaining data were divided into training and validation sets in an 8:2 ratio.

C. Model Training and Evaluation

The selection of the following experimental parameters is based on our experiments and experience. The optimal combination of parameters may vary for different datasets and problems.

¹[Online]. Available: https://github.com/a1025922331/Mars_Dust_Devil_Data_Set

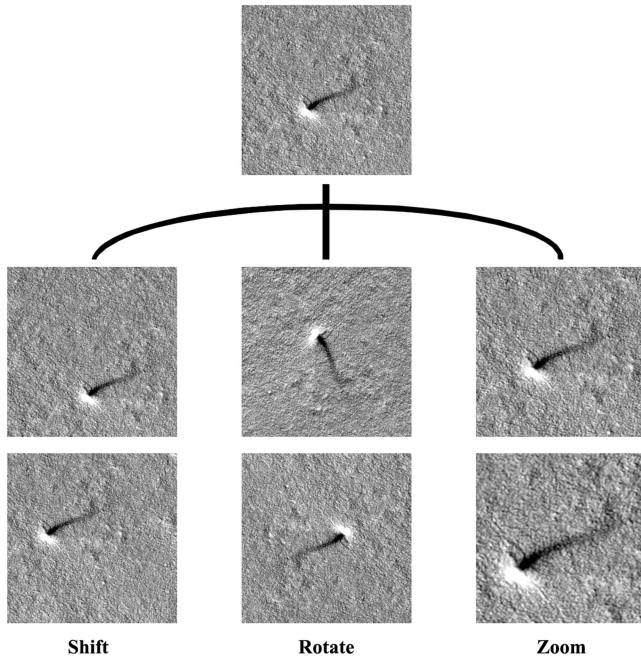


Fig. 11. Data augmentation diagram.

- 1) Initialize the parameters of the feature extraction network using the pretrained ResNet50 model trained on the ImageNet dataset. This is because ResNet50 has demonstrated excellent performance on large-scale image classification tasks and has strong feature extraction capabilities, which can provide a good initial feature representation for our model.
- 2) Set the training batch size to 16. Through experimentation, we have found that this batch size achieves a good balance between training speed and model performance.
- 3) Set the initial learning rate to 0.005. This value is determined by trying different learning rates and selecting the one that yields better convergence performance during training.
- 4) Set the number of training epochs to 100. Through experimental observation, we have found that within this number of epochs, the model can sufficiently learn the features of the data and achieve good performance.
- 5) Set the learning rate decay step to 30 and the learning rate decay rate to 0.1. This setting gradually reduces the learning rate during training to help the model converge better.
- 6) Set the threshold for NMS to 0.5 and the IoU threshold to 0.7. The threshold for NMS is used to suppress bounding boxes with significant overlap to obtain more accurate prediction results. The IoU threshold is used to determine the degree of overlap between candidate boxes and ground truth boxes to determine whether to treat them as positive or negative samples for training. In our experiments, the combination of an NMS threshold of 0.5 and an IoU threshold of 0.7 has shown good performance.

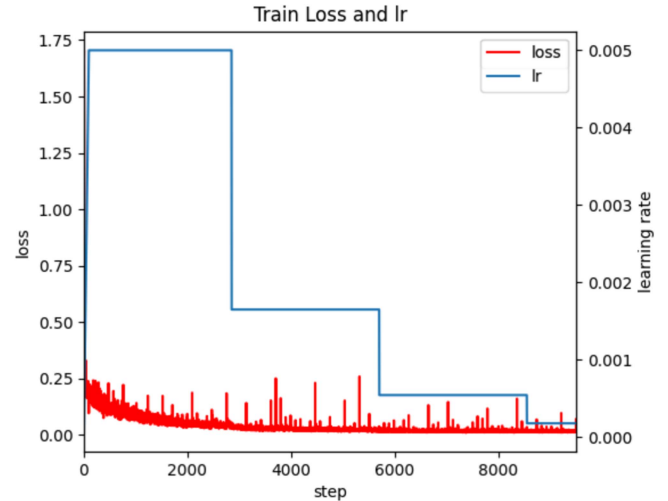


Fig. 12. Train loss and learning rate.

Using precision, recall, and average precision (AP) as evaluation metrics

$$R = \frac{TP}{TP + FN} \quad (6)$$

$$P = \frac{TP}{TP + FP} \quad (7)$$

$$AP = \int_0^1 P(R) dR. \quad (8)$$

TP represents the positive samples predicted to be positive; FN represents the positive samples predicted to be negative; and FP represents the negative samples predicted to be positive. $F(R)$ is the precision–recall curve.

D. Result Analysis

Using the constructed Martian dust devil detection dataset, we verified the detection performance of the MDDD Net algorithm proposed in this article. The changing trends of training loss and learning rate are shown in Fig. 12. It can be seen that the training loss decreases rapidly at the beginning and then gradually becomes flat, which indicates that the model has converged. The AP curve is shown in Fig. 13. Among them, the best score is the 9th epoch, whose average precision is 90.1% and recall is 96.5%.

The results of testing on the Martian dust devil detection dataset using the original faster R-CNN and other commonly used object detection algorithms are as follows. As can be seen from Table II, the MDDD Net proposed in this article achieves the best results in both the average precision and recall on Martian dust devil detection (Bold lines in Table II). Compared with the original faster R-CNN, the improved strategy proposed in this article has a significant effect, the AP is increased by 4.7%, and the recall is increased by 6.8%.

In terms of detection speed, although the aforementioned improvement methods have increased the computational complexity to some extent (especially with the introduction of the RPN), the reduction in frames per second (FPS) compared with

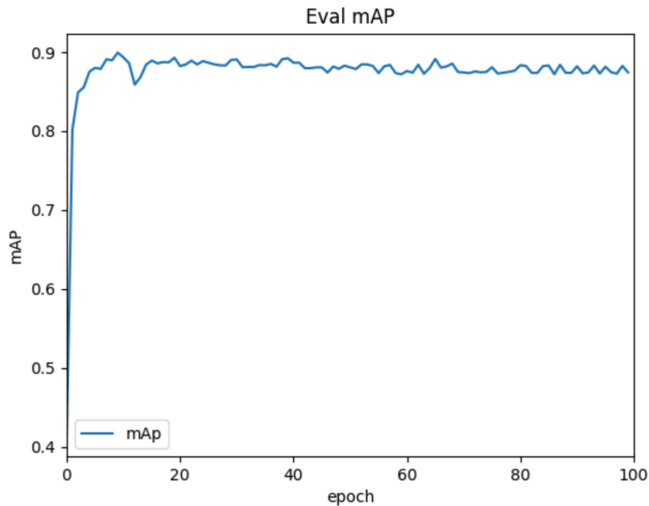


Fig. 13. AP curve.

TABLE II
PERFORMANCE COMPARISON BETWEEN DIFFERENT MODELS

Model	AP(%)	Recall(%)	FPS
SSD 300	72.4	65.6	27
YOLO v4	79.8	77.2	32
EfficientDet-D2	86.6	85.6	23
Fast R-CNN	68.4	70.9	7
Faster R-CNN	85.4	89.7	13
MDDD Net	90.1	96.5	12

the original faster R-CNN is negligible. The processing time per frame is approximately 83 ms, which is still high and meets the requirements for real-time processing. Taking the CTX image data used in the experiment as an example, it is possible to scan almost 241 km² of the Martian surface per second while maintaining high accuracy.

Furthermore, although the aforementioned improvement methods have increased the computational complexity to some extent (especially with the introduction of the RPN), the reduction in FPS compared with the original faster R-CNN is negligible. The processing time per frame is approximately 83 ms, which is still high and meets the requirements for real-time processing. Taking the CTX image data used in the experiment as an example, it is possible to scan almost 241 km² of the Martian surface per second while maintaining high accuracy. Compared with the traditional detection methods based on Gaussian filters [22], [23] and CNNs [27], MDDD Net achieves a 3–6 times improvement in detection latency.

In addition, we evaluated the four improvement strategies employed in this study by setting up independent experimental groups and conducting ablation experiments. The results of these experiments are presented in Table III. It is evident from the results that, compared with the other control groups, the improvement strategy based on FPN had the most significant impact on the model's performance (Bold lines in Table III).

TABLE III
ABLATION EXPERIMENTS

Method	AP(%)	Recall(%)
Base Line (Faster R-CNN)	85.4	89.7
FPN	88.9	94.3
K-means++	86.5	91.4
Soft-NMS	85.9	90.1
ROI Align	86.7	90.9

Specifically, the FPN improvement strategy resulted in a notable increase of 3.5% in average precision (AP) and 4.6% in recall. On the other hand, the other improvement strategies showed relatively smaller improvements in model performance. This can be attributed to the fact that these strategies primarily focused on optimizing specific scenarios, such as challenging positive and small sample size. Since these scenarios constitute a smaller proportion within the dataset, their impact on the model's validation results was consequently limited.

Fig. 14 shows a comparison of the detection results between MDDD Net and faster R-CNN on the test dataset. From Fig. 14(a) and (b), we can see that the detection effect of MDDD Net for small-sized dust devils is significantly improved, which indicates that the use of feature pyramids to fuse multiscale feature maps and the introduction of ROI align to solve feature map mapping deviations are effective. From Fig. 14(c) and (d), we can see that the dust devils with low dust density and at diffuse state are also accurately detected, which shows that the model has strong generalization ability, and the data augmentation methods used to prevent the overfitting are effective. From Fig. 14(e) and (f), we can see that MDDD Net shows a significant improvement in difficult negative instances, correctly avoiding the misclassification of small craters and hills that resemble dust devils. From Fig. 14(g), we can see that when multiple dust devils are adjacent and the bounding boxes overlap, the model also accurately detects all dust devils, which shows that the method of using soft-NMS to complete candidate box screening is wise. The above discussion also explains why MDDD Net has a large improvement in recall compared with the original faster R-CNN.

But from Fig. 14(h), we can also find that some dust devils are repeatedly detected. We think the main reason is that some dust devils are affected by surface winds and other factors, resulting in discontinuous dust columns, which makes it more difficult to define the boundaries of those dust devils. Although this situation will reduce the precision of the model to a certain extent, in the Martian dust devil detection task, we pay more attention to the recall than the precision. The detection results can be manually screened for a second time to eliminate a small number of false positive objects.

In addition to testing with the Amazonis Planitia dataset, we constructed a small supplementary test set consisting of 80 non-Azonis Planitia images (such as Utopia Planitia, Deuteronilus Mensae, and Xanthe Terra) to evaluate the generalization ability and robustness of our model in the field of object detection. These images encompassed three different devices: CRISM,

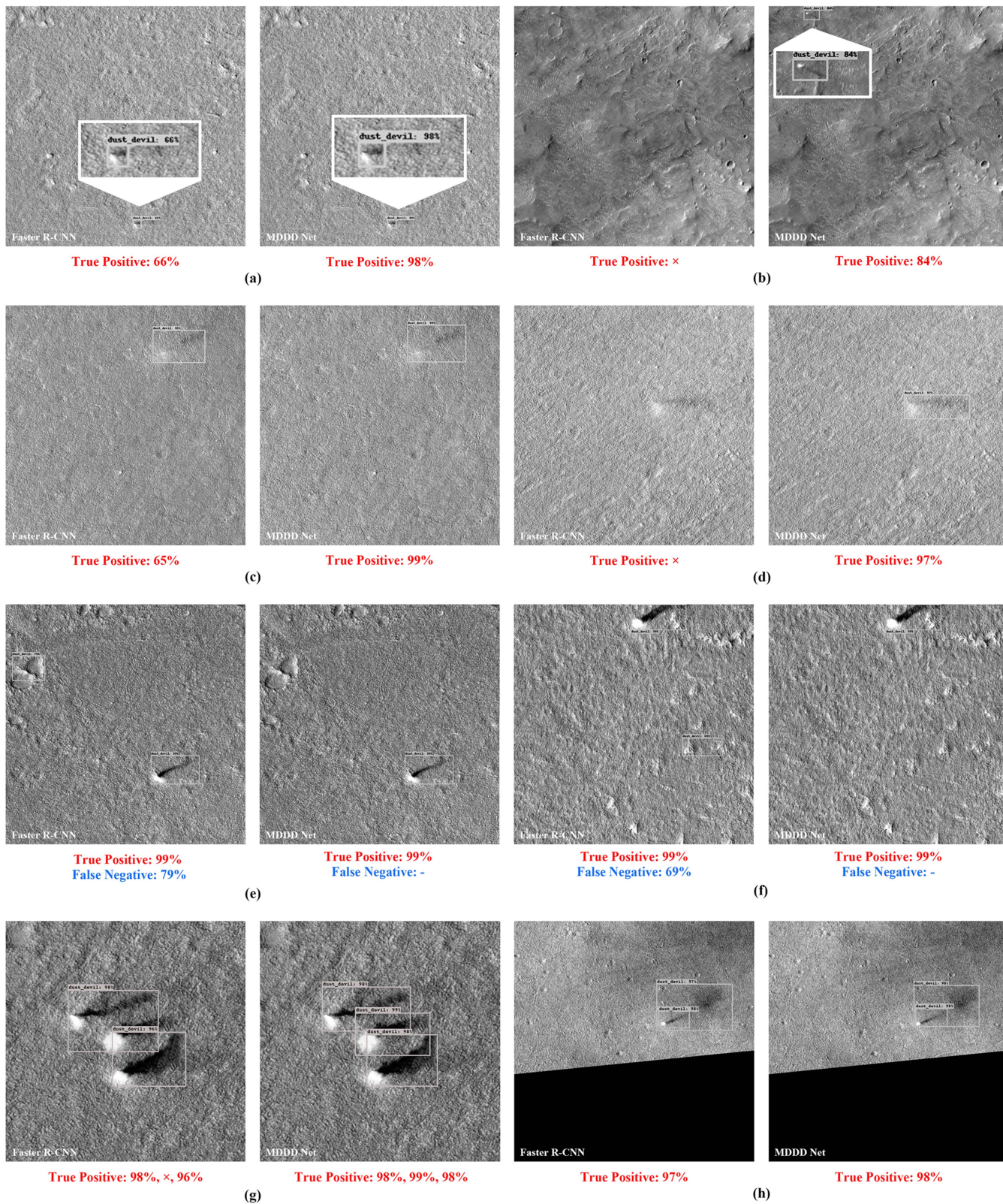


Fig. 14. Detection results comparison (faster R-CNN versus MDDD Net). (a) and (b) Small-size dust devils. (c) and (d) Dust devils with low dust density and at diffuse state. (e) and (f) Hard negatives. (g) Dense dust devils. (h) Dust devils that are repeatedly detected.

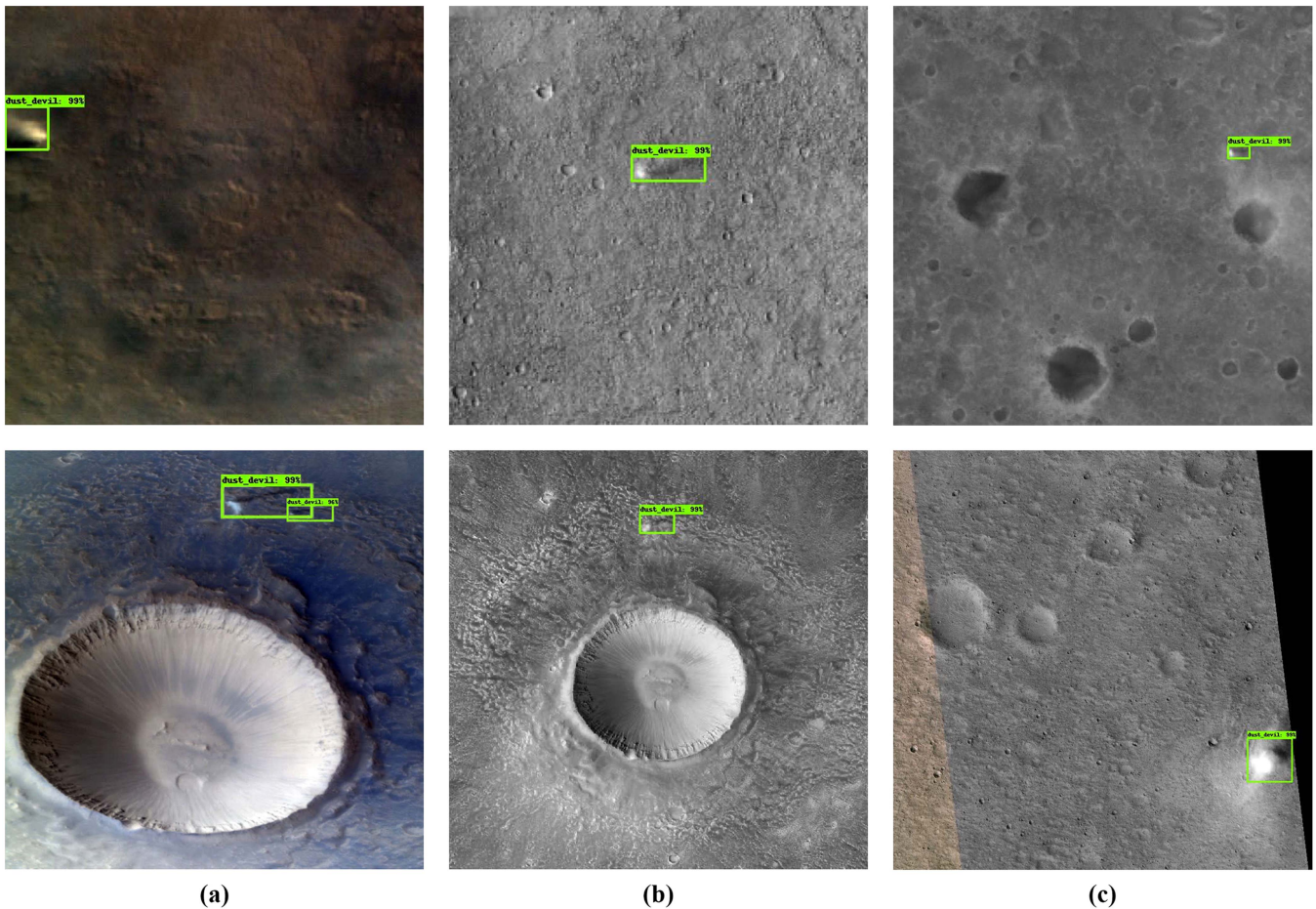


Fig. 15. Detection results on the supplementary test set. (a) CRISM. (b) CTX. (c) HiRISE.

TABLE IV
EVALUATION RESULTS OF THE SMALL ADDITIONAL TEST SET

Instruments	AP(%)	Recall(%)
CTX	91.7	95.1
HiRISE	78.6	88.3
CRISM	69.4	79.2

CTX, and HiRISE. The test results, as shown in Fig. 15 and Table IV, indicate that when tested with non-Azonis Planitia CTX images, the model's performance closely approximated the evaluation results obtained from the Azonis Planitia test set. Moreover, testing on CRISM and HiRISE images also yielded favorable results, further highlighting the strong generalization ability and robustness of the MDDD Net.

In short summary, the MDDD Net proposed in this article improves the detection ability of dust devil objects from Mars orbiter images.

E. Limitations and Future Work

This study has made progress in automatic dust devil detection. However, there are still limitations and areas for further exploration. Specifically, they are as follows.

- 1) The performance of deep learning object detection models heavily depends on the quality and diversity of the dataset. The environment on Mars is highly complex and variable, with dust devils having different sizes and shapes. They can also be easily confused with small hills and crater pits. Due to the current limitation of utilizing only the available images, constructing a more diverse and larger dataset becomes challenging. Hence, we plan to utilize generative adversarial networks [40] to generate a portion of Martian dust devil images in the future, in order to augment the dataset and further improve the model's generalization ability and detection accuracy.
- 2) This article solely focuses on the automatic recognition of dust devils. In the future, we intend to employ additional image processing methods to extract certain physical attributes of the detected dust devils, such as using the shadow method to calculate their heights [8]. This will provide multidimensional data for subsequent dust devil research, facilitating a deeper understanding of their characteristics and behavior.

By taking these measures, we aim to overcome the current limitations of the study, enhance the performance of the model, improve the accuracy of dust devil detection, and contribute to a more comprehensive understanding of dust devils through

the provision of comprehensive data in the field of dust devil research.

V. CONCLUSION

Based on the faster R-CNN network, we made several modifications according to the characteristics of the Martian dust devil detection task and proposed an MDDD Net. The main improvements are shown as follows.

- 1) The FPN is used to fuse the feature maps of all levels extracted in the ResNet50 feature extraction network to obtain feature fusion maps with rich location information and semantic information.
- 2) The k-means++ algorithm is used to design more reasonable prior anchor boxes to adapt to the morphological characteristics of the dust devil.
- 3) The RoI align unit proposed in the mask R-CNN algorithm is introduced to eliminate the mapping deviation between the feature maps and the original images.
- 4) The soft-NMS algorithm is used instead of the NMS algorithm to complete the screening of candidate boxes, which solves the problem of missing detection caused by mutual suppression between the adjacent dust devil candidate boxes in the same image.

With the Martian dust devil dataset, compared with the original faster R-CNN network, the MDDD Net network improves AP by 4.7% and recall by 6.8%, respectively. At the same time, it effectively solves the problems of poor generalization ability, low detection efficiency, and low accuracy of the traditional Martian dust devil automatic detection algorithm, and achieves the expected detection effect. It has reference significance for subsequent research on extracting the characteristics of Martian dust devils based on big data.

REFERENCES

- [1] C. F. Capen and L. J. Martin, "The developing stages of the Martian yellow storm of 1971," *Lowell Observatory Bulletin*, 1971, Accessed on: Dec. 28, 2021. [Online]. Available: http://www.researchgate.net/publication/234282720_The_developing_stages_of_the_Martian_yellow_storm_of_1971
- [2] R. J. Mckim, "Meeting contribution: Recent views of Mars," *J. Brit. Astron. Assoc.*, vol. 109, 1999, Art. no. 287.
- [3] B. A. Cantor, K. M. Kanak, and K. S. Edgett, "Mars orbiter camera observations of Martian dust devils and their tracks (September 1997 to January 2006) and evaluation of theoretical vortex models," *J. Geophysical Res. Planets*, vol. 111, no. E12, Dec. 2006, Art. no. E12002, doi: [10.1029/2006JE002700](https://doi.org/10.1029/2006JE002700).
- [4] J. A. Fisher et al., "A survey of Martian dust devil activity using Mars global surveyor Mars orbiter camera images," *J. Geophysical Res. Planets*, vol. 110, no. 3, 2005, Art. no. E03004, doi: [10.1029/2003JE002165](https://doi.org/10.1029/2003JE002165).
- [5] M. Balme and R. Greeley, "Dust devils on Earth and Mars," *Rev. Geophysical*, vol. 44, no. 3, 2006, Art. no. RG3003, doi: [10.1029/2005RG000188](https://doi.org/10.1029/2005RG000188).
- [6] T. Statella, P. Pina, and E. A. da Silva, "Image processing algorithm for the identification of Martian dust devil tracks in MOC and HiRISE images," *Planet. Space Sci.*, vol. 70, no. 1, pp. 46–58, Sep. 2012, doi: [10.1016/j.pss.2012.06.003](https://doi.org/10.1016/j.pss.2012.06.003).
- [7] R. W. Zurek, J. R. Barnes, R. M. Haberle, J. B. Pollack, and C. B. Leovy, "Dynamics of the atmosphere of Mars," *Mars*, 1992, Accessed on: Dec. 30, 2021. [Online]. Available: http://www.researchgate.net/publication/23868144_Dynamics_of_the_atmosphere_of_Mars
- [8] L. K. Fenton and R. Lorenz, "Dust devil height and spacing with relation to the Martian planetary boundary layer thickness," *Icarus*, vol. 260, pp. 246–262, Nov. 2015, doi: [10.1016/j.icarus.2015.07.028](https://doi.org/10.1016/j.icarus.2015.07.028).
- [9] C. Stanzel et al., "Dust devil speeds, directions of motion and general characteristics observed by the Mars express high resolution stereo camera," *Icarus*, vol. 197, no. 1, pp. 39–51, Sep. 2008, doi: [10.1016/j.icarus.2008.04.017](https://doi.org/10.1016/j.icarus.2008.04.017).
- [10] T. Peter and P. J. Gierasch, "Dust devils on Mars," 1985, Accessed on: Jan. 2, 2022. [Online]. Available: <http://arch.neicon.ru/xmlui/handle/123456789/2493029>
- [11] M. C. Malin and K. S. Edgett, "Mars global surveyor Mars orbiter camera: Interplanetary cruise through primary mission," *J. Geophysical Res. Planets*, vol. 106, no. E10, pp. 23429–23570, 2001, doi: [10.1029/2000JE001455](https://doi.org/10.1029/2000JE001455).
- [12] G. E. Cushing, T. N. Titus, and P. R. Christensen, "THEMIS VIS and IR observations of a high-altitude Martian dust devil," *Geophysical Res. Lett.*, vol. 32, no. 23, pp. 340–353, 2005, doi: [10.1029/2005GL024478](https://doi.org/10.1029/2005GL024478).
- [13] K. A. Milam et al., "THEMIS characterization of the MER Gusev crater landing site," *J. Geophysical Res. Planets*, vol. 108, no. E12, 2003, Art. no. 8078, doi: [10.1029/2002JE002023](https://doi.org/10.1029/2002JE002023).
- [14] D. S. Choi and C. M. Dundas, "Measurements of Martian dust devil winds with HiRISE," *Geophysical Res. Lett.*, vol. 38, no. 24, 2011, Art. no. L24206, doi: [10.1029/2011gl049806](https://doi.org/10.1029/2011gl049806).
- [15] F. Ferri, P. H. Smith, M. Lemmon, and N. O. Rennó, "Dust devils as observed by Mars pathfinder," *J. Geophysical Res.*, vol. 108, Dec. 2003, Art. no. 5133, doi: [10.1029/2000JE001421](https://doi.org/10.1029/2000JE001421).
- [16] R. Greeley, "Gusev crater: Wind-related features and processes observed by the Mars exploration rover spirit," *J. Geophysical Res. Atmos.*, vol. 111, 2006, Art. no. E02S09, doi: [10.1029/2005je002491](https://doi.org/10.1029/2005je002491).
- [17] R. Greeley et al., "Gusev crater, Mars: Observations of three dust devil seasons," *J. Geophysical Res. Planets*, vol. 115, no. E7, 2010, Art. no. E00F02, doi: [10.1029/2010JE003608](https://doi.org/10.1029/2010JE003608).
- [18] S. M. Metzger, J. R. Carr, J. R. Johnson, T. J. Parker, and M. T. Lemmon, "Dust devil vortices seen by the Mars pathfinder camera," *Geophysical Res. Lett.*, vol. 26, no. 18, pp. 2781–2784, 1999.
- [19] S. M. Metzger, J. R. Carr, J. R. Johnson, T. J. Parker, and M. T. Lemmon, "Techniques for identifying dust devils in Mars pathfinder images," *IEEE Trans. Geosci. Remote Sens.*, vol. 38, no. 2, pp. 870–876, Mar. 2000, doi: [10.1109/36.842015](https://doi.org/10.1109/36.842015).
- [20] J. E. Moores et al., "Observational evidence of a suppressed planetary boundary layer in Northern gale crater, Mars as seen by the Navcam instrument onboard the Mars science laboratory rover," *Icarus*, vol. 249, pp. 129–142, Mar. 2015, doi: [10.1016/j.icarus.2014.09.020](https://doi.org/10.1016/j.icarus.2014.09.020).
- [21] A. Castano et al., "Automatic detection of dust devils and clouds on Mars," *Mach. Vis. Appl.*, vol. 19, no. 5/6, pp. 467–482, Oct. 2008, doi: [10.1007/s00138-007-0081-3](https://doi.org/10.1007/s00138-007-0081-3).
- [22] F. Yang, P. A. Mlsna, and P. Geissler, "Gaussian-based filters for detecting Martian dust devils," in *Proc. IEEE Southwest Symp. Image Anal. Interpretation*, 2006, pp. 46–50, doi: [10.1109/SSIAI.2006.1633719](https://doi.org/10.1109/SSIAI.2006.1633719).
- [23] A. Gibbons, F. Yang, P. Mlsna, and P. E. Geissler, "Automated procedures for detecting Martian dust devils," in *Proc. Lunar Planet. Sci. Conf.*, 2005, Accessed on: Dec. 27, 2021. [Online]. Available: <http://adsabs.harvard.edu/abs/2005LPI....36.2005G>
- [24] M. R. Balme, P. L. Whelley, and R. Greeley, "Mars: Dust devil track survey in Argyre Planitia and Hellas basin," *J. Geophysical Res. Planets*, vol. 108, no. E8, 2003, Art. no. 5086, doi: [10.1029/2003JE002096](https://doi.org/10.1029/2003JE002096).
- [25] I. J. Daubar et al., "Global distribution of dust devil tracks in HiRISE images," in *Proc. 51st Annu. Lunar Planet. Sci. Conf.*, no. 2326, Mar. 2020, Art. no. 2207. [Online]. Available: <https://ui.adsabs.harvard.edu/abs/2020LPI....51.2207D/abstract>
- [26] D. Reiss, N. M. Hoekzema, and O. J. Stenzel, "Dust deflation by dust devils on Mars derived from optical depth measurements using the shadow method in HiRISE images," *Planet. Space Sci.*, vol. 93–94, pp. 54–64, Apr. 2014, doi: [10.1016/j.pss.2014.01.016](https://doi.org/10.1016/j.pss.2014.01.016).
- [27] R. Woollands et al., "Maximizing dust devil follow-up observations on Mars using CubeSats and on-board scheduling," *J. Astronaut. Sci.*, vol. 69, pp. 918–940, 2022, doi: [10.1007/s40295-022-00317-z](https://doi.org/10.1007/s40295-022-00317-z).
- [28] D. Brown, W. C. Huffman, H. Sierks, D. R. Thompson, and S. A. Chien, "Automatic detection and tracking of plumes from 67P/Churyumov-Gerasimenko in Rosetta/OSIRIS image sequences," *Astron. J.*, vol. 157, no. 1, 2019, Art. no. 27, doi: [10.1002/2015gl064500](https://doi.org/10.1002/2015gl064500).
- [29] T. J. Fuchs et al., "Enhanced flyby science with onboard computer vision: Tracking and surface feature detection at small bodies," *Earth Space Sci.*, vol. 2, no. 10, pp. 417–434, 2016, doi: [10.1002/2014EA000042](https://doi.org/10.1002/2014EA000042).
- [30] D. R. Thompson, M. Bunte, R. Castano, S. Chien, and R. Greeley, "Image processing onboard spacecraft for autonomous plume detection," *Planet. Space Sci.*, vol. 62, no. 1, pp. 153–159, 2012, doi: [10.1016/j.pss.2011.11.006](https://doi.org/10.1016/j.pss.2011.11.006).

- [31] “Data on artificial intelligence reported by researchers at University of Pisa (the phi-sat-1 mission: The first on-board deep neural network demonstrator for satellite Earth observation),” *Netw. Dly. News*, Apr. 2022. Accessed on: Jan. 24, 2024. [Online]. Available: https://www.nstl.gov.cn/paper_detail.html?id=28e84e626a5c11ecd207a6dd7e79f9cd
- [32] E. Dunkel et al., “Benchmarking deep learning inference of remote sensing imagery on the Qualcomm snapdragon and intel Movidius myriiad X processors onboard the international space station,” in *Proc. IEEE Int. Geosci. Remote Sens. Symp.*, 2022, pp. 5301–5304.
- [33] S. Ren, K. He, R. Girshick, and J. Sun, “Faster R-CNN: Towards real-time object detection with region proposal networks,” *IEEE Trans. Pattern Anal. Mach. Intell.*, vol. 39, no. 6, pp. 1137–1149, Jun. 2017, doi: [10.1109/TPAMI.2016.2577031](https://doi.org/10.1109/TPAMI.2016.2577031).
- [34] C. Szegedy et al., “Going deeper with convolutions,” in *Proc. IEEE Conf. Comput. Vis. Pattern Recognit.*, 2015, pp. 1–9, doi: [10.1109/CVPR.2015.7298594](https://doi.org/10.1109/CVPR.2015.7298594).
- [35] K. He, X. Zhang, S. Ren, and J. Sun, “Deep residual learning for image recognition,” in *Proc. IEEE Conf. Comput. Vis. Pattern Recognit.*, 2016, pp. 770–778, doi: [10.1109/CVPR.2016.90](https://doi.org/10.1109/CVPR.2016.90).
- [36] T.-Y. Lin, P. Dollár, R. Girshick, K. He, B. Hariharan, and S. Belongie, “Feature pyramid networks for object detection,” in *Proc. IEEE Conf. Comput. Vis. Pattern Recognit.*, 2017, pp. 936–944, doi: [10.1109/CVPR.2017.106](https://doi.org/10.1109/CVPR.2017.106).
- [37] N. Bodla, B. Singh, R. Chellappa, and L. S. Davis, “Soft-NMS—Improving object detection with one line of code,” 2017. Accessed on: Jan. 12, 2022. [Online]. Available: <http://arxiv.org/abs/1704.04503v2>
- [38] K. He, G. Gkioxari, P. Dollár, and R. Girshick, “Mask R-CNN,” *IEEE Trans. Pattern Anal. Mach. Intell.*, vol. 42, no. 2, pp. 386–397, Feb. 2020, doi: [10.1109/TPAMI.2018.2844175](https://doi.org/10.1109/TPAMI.2018.2844175).
- [39] D. Reiss, A. Spiga, and G. Erkeling, “The horizontal motion of dust devils on Mars derived from CRISM and CTX/HiRISE observations,” *Icarus*, vol. 227, pp. 8–20, Jan. 2014, doi: [10.1016/j.icarus.2013.08.028](https://doi.org/10.1016/j.icarus.2013.08.028).
- [40] T. Karras, T. Aila, S. Laine, and J. Lehtinen, “Progressive growing of GANs for improved quality, stability, and variation,” 2017, *arXiv:1710.10196*.



Dagang Li received the bachelor’s degree in telecommunication engineering from the Huazhong University of Science and Technology, Wuhan, China, in 1998, and the Ph.D. degree in electrical engineering from Katholieke Universiteit Leuven, Leuven, Belgium, in 2010.

He is currently an Assistant Professor with the Macau University of Science and Technology, Macau, China. His research interests include computer networks, data processing, and artificial intelligence.



Yemeng Wang received the B.Sc. degree in environmental science from Huaqiao University, Xiamen, China, in 2017, and the M.Sc. and Ph.D. degrees in Earth and planetary science from the Macau University of Science and Technology, Macau, China, in 2019 and 2023, respectively.

Her research interest is the numerical simulation of the Martian atmosphere.



Kim-Chiu Chow received the Ph.D. degree in mathematics from the Hong Kong University of Science and Technology, Hong Kong, in 2001.

He is currently an Assistant Professor with the Macau University of Science and Technology, Macau, China. His research is mainly about the atmospheres of Earth and Mars, particularly on the dynamics and climate of dust storms in recent years.



Zexin Guo received the B.Sc. degree in applied physics from the College of Physics and Energy, Shenzhen University, Shenzhen, China, in 2020, and the M.Sc. degree in Space Big Data Analytics in Macau University of Science and Technology, Macau, China, in 2022.

His research interests include the processing of remote sensing image data and deep learning.



Renrui Liu received the B.S. degree in optoelectronic information science and engineering from the School of Physics and Optoelectronic Engineering, Shandong University of Technology, Zibo, China, in 2020, and the M.S. degree in space big data analytics in 2022 from the State Key Laboratory of Lunar and Planetary Sciences, Macau University of Science and Technology, Macau, China, where he is currently working toward the Ph.D. degree in earth and planetary sciences.

His research interests include deep learning, 3-D modeling, image processing, and GPR data processing.



Yi Xu (Member, IEEE) received the B.S. degree in physics from Nanjing University, Nanjing, China, in 2004, and the M.S. degree in microelectronics and the Ph.D. degree in electrical and computer engineering from the University of Pittsburgh, Pittsburgh, PA, USA, in 2007 and 2012, respectively.

She is currently an Associate Professor with Space Science Institute, Macau University of Science and Technology, Macau, China. Her research interests include microwave and radar data processing, planetary geology, computer architecture, and on-chip network design.



Qiquan Yang received the B.S. degree in survey and mapping, and the Ph.D. degree in photogrammetry and remote sensing from Wuhan University, Wuhan, China, in 2016 and 2021, respectively.

He is currently a Postdoctoral Researcher affiliated with both Macau University of Science and Technology, Macau, China, and Tongji University, Shanghai, China. He has authored more than ten peer-reviewed papers in international journals. He is mainly engaged in infrared remote sensing data processing and analysis, including surface thermal environment modeling and planetary surface water infrared detection.